A Linearized Fit Model for Robust Shape Parameterization of FET-PET TACs

Christoph W, Lerche, Timon Radomski, Philipp Lohmann, Liliana Caldeira, Cláudia Régio Brambilla, Lutz Tellmann, Jürgen Scheins, Elena Rota Kops, Norbert Galldiks, Karl-Josef Langen, Hans Herzog, N.Jon Shah

Abstract—The kinetic analysis of 18F-FET time-activity curves (TAC) can provide valuable diagnostic information in glioma patients. The analysis is most often limited to the average TAC over a large tissue volume and is normally assessed by visual inspection or by evaluating the time-topeak and linear slope during the late uptake phase. Here, we derived and validated a linearized model for TACs of ¹⁸F-FET in dynamic PET scans. Emphasis was put on the robustness of the numerical parameters and how reliably automatic voxel-wise analysis of TAC kinetics was possible. The diagnostic performance of the extracted shape parameters for the discrimination between isocitrate dehydrogenase (IDH) wildtype (wt) and IDH-mutant (mut) glioma was assessed by receiver-operating characteristic in a group of 33 adult glioma patients. A high agreement between the adjusted model and measured TACs could be obtained and relative, estimated parameter uncertainties were small. The best differentiation between IDH-wt and IDH-mut gliomas was achieved with the linearized model fitted to the averaged TAC values from dynamic FET PET data in the time interval 4-50 min p.i.. When limiting the acquisition time to 20-40 min p.i., classification accuracy was only slightly lower (-3%) and was comparable to classification based on linear fits in this time interval. Voxel-wise fitting was possible within a computation time ≈ 1 min per image slice. Parameter uncertainties smaller than 80% for all fits with the linearized model were achieved. The agreement of best-fit parameters when comparing voxelwise fits and fits of averaged TACs was very high (p<0.001).

Index Terms— FET PET, glioma classification, parametric imaging.

I. INTRODUCTION

URRENTLY, one of the most commonly used tracer for brain tumor diagnosis in western Europe is ¹⁸F-FET [1]. The clinical impact of ¹⁸F-FET has been demonstrated by its applicability in the delineation of glioma extent for biopsy guidance and radiotherapy planning, the differentiation of actual tumor relapse from treatment-related changes, and treatment response assessment. In addition, several studies have demonstrated that dynamic changes in ¹⁸F-FET accumulation in gliomas during the first hour after injection are correlated with the malignancy of the lesion. For example, the IDH-wt glioblastoma, which is one of the most aggressive brain tumors, is characterized by an early peak around 10-15 min after injection followed by a decreasing uptake, whereas less malignant brain tumors, such as the IDH-mut diffuse astrocytoma of grade II (according to the World Health Organization (WHO)) of the Central Nervous System [2] show a constantly increasing tracer uptake [3], [4]. Using the dynamic evaluation of tumors, grade II and grade IV gliomas (according to the WHO classification of 2007 [2]) could be distinguished with an accuracy > 90% in both newly diagnosed and recurrent gliomas [5], [6]. The different kinetics of tracer uptake in relation to the malignancy of the tumor appears to be a specific property of ¹⁸F-FET. Potential differences in the malignancy-

- C.W. Lerche is with the Institute of Neuroscience and Medicine 4, Forschungszentrum Jülich, Germany (e-mail: c.lerche@fz-juelich.de).
- T. Radomski is with the Institute of Neuroscience and Medicine 4, Forschungszentrum Jülich, Germany (e-mail: t.radomski@fz-juelich.de).
- P. Lohmann is with the Institute of Neuroscience and Medicine 4, Forschungszentrum Jülich, Germany and the Department of Stereotaxy and Functional Neurosurgery, Faculty of Medicine and University Hospital Cologne, University of Cologne, Cologne, Germany (e-mail: p.lohmann@fz-juelich.de).
- C. Régio Brambilla is with the Institute of Neuroscience and Medicine 4, Forschungszentrum Jülich, Germany (e-mail: c.regio-brambilla@fz-juelich.de).
- L. Tellmann is with the Institute of Neuroscience and Medicine 4, Forschungszentrum Jülich, Germany (e-mail: I.tellmann@fz-juelich.de).
- J. Scheins is with the Institute of Neuroscience and Medicine 4, Forschungszentrum Jülich, Germany (e-mail: j.scheins@fz-juelich.de).
- E. Rota Kops is with the Institute of Neuroscience and Medicine 4, Forschungszentrum Jülich, Germany (e-mail: e.rota.kops@fz-juelich.de).
- K.-J. Langen is with the Institute of Neuroscience and Medicine 4, Forschungszentrum Jülich, Jülich, Germany and with the Center of Integrated Oncology (CIO), Universities Aachen, Bonn, Duesseldorf and Cologne, Germany (e-mail: k.i.langen@fz-juelich.de).
- H. Herzog is with the Institute of Neuroscience and Medicine 4, Forschungszentrum Jülich, Germany (e-mail: h.herzog@fz-juelich.de).
- L. Caldeira was with the Institute of Neuroscience and Medicine 4, Forschungszentrum Jülich, Jülich, Germany. She is now with the Institute of Diagnostic and Interventional Radiology, University of Cologne, Cologne, Germany, (e-mail: liliana.lourenco-caldeira@uk-koeln.de).
- N. Galldiks is with the Institute of Neuroscience and Medicine 3, Forschungszentrum Jülich, Jülich, Germany; the Department of Neurology, Faculty of Medicine and University Hospital Cologne, University of Cologne, Cologne, Germany; and the Center of Integrated Oncology (CIO), Universities Aachen, Bonn, Duesseldorf and Cologne, Germany (e-mail: Norbert.Galldiks@uk-koeln.de).
- N. J. Shah is with the Institutes of Neuroscience and Medicine 4 and 11, Forschungszentrum Jülich, Germany; JARA BRAIN Translational Medicine, Aachen, Germany; the Department of Neurology, RWTH Aachen University, Aachen, Germany (e-mail: n.i.shah@fz-juelich.de).

dependent kinetics of tracer uptake for ¹¹C-MET and ¹⁸F-FDOPA PET are still under discussion [7]–[10].

There are several possibilities for quantifying the uptake kinetics of ¹⁸F-FET. However, all approaches are subject to different methodological hurdles. First, dynamic ¹⁸F-FET imaging requires a longer acquisition time, which is generally incompatible with clinical routine and reduces the number of patients that can be investigated with one batch of synthesized ¹⁸F-FET, thus leading to increased costs. Second, the extraction of parameters sufficiently describing the dynamic uptake behavior is either complex, subjective, or highly simplified. Kinetic modeling is the most accurate approach and allows rate constants to be quantified in a 2-tissue compartment model [7], [11], [12]. However, compartment modeling is very elaborate and requires the commencement of dynamic PET acquisitions with the injection of the tracer. It also requires the determination of the arterial input function, either derived from the image or by taking blood samples [12]. Alternatively, the time-to-peak value (TTP; time from the injection of the tracer until reaching the maximum of the time-activity curve (TAC)) can be used or the slope of the TAC can be determined by fitting a linear function of time to the late phase of the TAC. The definition of the late phase differs between authors and refers to either 20-50 min post-injection (p.i.) or to 15-40 min p.i. [4], [13]. However, the drawbacks of these methods are that ¹⁸F-FET TAC data are only partially used and that the ¹⁸F-FET TAC is not linear. Classification into three TAC types, either by nonsupervised k-means clustering or by trained human observers, has also been proposed [14], [15]. The main limitation of the clustering approach is the discretization into a small number of predefined uptake behaviors, which may not classify potential intermediate curve patterns appropriately.

In addition to the classification of the entire tumor, imaging of locally differing tumor characteristics is also of interest, since one intrinsic property of gliomas is a pronounced intratumoral heterogeneity [16], and information relating to this is highly relevant for prognosis [17]. Regionally different ¹⁸F-FET uptake kinetics have been observed in heterogeneous gliomas during the first 50 min p.i., indicating different grades of malignancy within the same tumor [18]. Voxel-wise assessment of the radiotracer kinetics potentially allows for parametric imaging of regional malignancy in heterogeneous gliomas. Linear regression and non-supervised k-means classification are, to date, the only methods that have been implemented to extract the characteristics of ¹⁸F-FET uptake on a voxel level [13], [16], [19].

The aim of this work was to identify an explicit linearized model that is able to reproduce the different uptake kinetics of ¹⁸F-FET with high accuracy. The model must be able to map the different kinetic behavior in healthy brain tissue, IDH-mut, and

IDH-wt gliomas, onto different numerical values of one objective, single model parameter with low numerical uncertainty. Furthermore, the model should utilize the TAC data, either entirely when it is possible, or partially otherwise, without substantial differences in the numerical values of the shape parameter and the fitting should be robust enough to enable fast and automatic voxel-wise processing with minimal user interaction. We validated the model in a group of 33 adult patients with histomolecularly characterized primary (n=32) or recurrent cerebral glioma (n=1) according to the revised WHO classification 2016 of Tumors of the Central Nervous System [20]. We also verified the feasibility and predictive value of this approach on the same patient cohort.

II. METHODS AND MATERIALS

A. Linearized model for ¹⁸F-FET uptake kinetics

The derivation of the linearized model for the description of ¹⁸F-FET TACs was motivated by the observation that analytic models such as the Bateman-Function for pharmacokinetic processes [21],

$$c(t) = f \frac{D}{V} \frac{k_a}{k_a - k_e} (e^{-k_e t} - e^{-k_a t}), \tag{1}$$

and the more general double exponential model [21],

$$c(t) = E \cdot e^{-k_e t} - A \cdot e^{-k_a t}, \tag{2}$$

are inadequate. In these equations, c(t) is the substance concentration, k_a is the absorption rate, k_e is the elimination rate, D is the dose, V is the distribution volume, f is the bioavailability, A is the y-intercept of the distribution phase, and E is the y-intercept of the elimination phase [21]. These models have three and four free fit parameters, respectively, leading to less stable parameter estimates with large uncertainties in the case of (2) or, in the case of (1), to inaccurate TAC modeling. To find a suitable, alternative, linearized model with only two free parameters, we made several general and heuristic assumptions: 1) the function $u: R \to R_0^+$ maps the time t to the ¹⁸F-FET uptake in a single image voxel or a volume of interest (VOI) consisting of several image voxels. The uptake values can be given as activity concentration, standardized uptake value (SUV), or bare counts; 2) u(t) is non-negative for $t_{injection} \leq t$, where $t_{injection}$ is the injection time of the radiotracer, which can be set to zero without loss of generality; 3) since ¹⁸F-FET TACs with more than 1 maximum have not been reported to date, u(t) is supposed to have exactly one global maximum for $t > t_{injection} = 0$. As all PET measurements must be stopped at a time $t_{acquistion} < \infty$, the global maximum may be unobserved during the time $0 \le t \le$ $t_{acquisition}$; 4) for physical reasons, u(t=0)=0. A general class of functions with three free parameters A, κ, β , which fulfills all four required conditions for A, κ , $\beta > 0$, is given by

$$u(t) = At^{\beta} e^{-\kappa \cdot t^{\beta}} \tag{3}$$

A represents the amplitude of the tracer uptake, while κ and β are shape parameters influencing the TTP and the decay of u(t) after reaching the maximum. In addition, β defines the slope of

TABLE I: HISTOMOLECULAR DATA OF ALL PATIENTS TOGETHER WITH RESULTS FROM CHI² FITS. ^APATTERN OF THE TAC. FOR DEFINITION OF PATTERNS, SEE TEXT.
^BHISTOLOGICAL DIAGNOSIS AFTER SURGERY OR BIOPSY: A II = ASTROCYTOMA WHO GRADE II, A III = ANAPLASTIC ASTROCYTOMA WHO GRADE III, ODG II =

OLIGODENDROGLIOMA WHO GRADE II, ODG III = ANAPLASTIC OLIGODENDROGLIOMA WHO GRADE III, GBM = GLIOBLASTOMA, C TREATMENT: OP – OPERATION, R – RADIOTHERAPHY WITH CONCOMITANT TEMOZOLOMIDE CHEMOTHERAPY, CH – ADJUVANT TEMOZOLOMIDE CHEMOTHERAPY. D Y-INTERCEPT OF THE LINEAR FUNCTION, E SLOPE OF THE LINEAR FUNCTION, E TTP = TIME-TO-PEAK OF THE TAC FROM FIT WITH THE LINEARIZED TAC MODEL.

No.	Sex	Age [y]	Pat.A	IDH	Hist.B	Treatment ^C	t ^D [g/ml]	m ^E [10-4/s]	χ^2/ν	ln(A) [ln(g/ml)]	κ [10-2/√s]	χ^2/ν	TTP _{Fit} ^F [min]
1	M	51	f	wt	GBM	none	2.6 ± 0.06	-2.94 ± 0.27	1.41	-1.691 ± 0.023	3.24 ± 0.06	1.24	15.9 ± 0.6
2	F	67	f	wt	GBM	none	3.83 ± 0.05	-3.59 ± 0.22	1.74	-1.52 ± 0.03	2.68 ± 0.09	1.24	23.3 ± 1.5
3	F	58	f	wt	GBM	none	2.535 ± 0.026	-0.7 ± 0.12	1.34	-1.852 ± 0.007	2.512 ± 0.019	1.19	26.4 ± 0.4
4	M	54	f	wt	GBM	none	2.12 ± 0.07	-2.4 ± 0.3	1.62	-1.757 ± 0.028	3.53 ± 0.08	1.31	13.4 ± 0.6
5	F	66	f	wt	A II	none	2.65 ± 0.3	-2.4 ± 1.4	1.49	-2.23 ± 0.1	1.89 ± 0.26	1.27	47. ± 13.
6	M	55	f	wt	GBM	none	4.31 ± 0.11	-3.3 ± 0.5	1.65	-1.53 ± 0.03	2.38 ± 0.09	1.23	29.5 ± 2.2
7	M	39	f	wt	GBM	none	3.03 ± 0.04	-1.77 ± 0.19	1.32	-1.507 ± 0.015	3.01 ± 0.04	1.22	18.4 ± 0.5
8	F	68	f	wt	GBM	none	3.05 ± 0.04	$-3. \pm 0.17$	1.54	-1.542 ± 0.016	3.15 ± 0.04	1.29	16.8 ± 0.4
9	M	54	f	wt	GBM	none	2.5 ± 0.04	-1.91 ± 0.18	1.37	-1.761 ± 0.015	2.99 ± 0.04	1.21	18.6 ± 0.5
10	F	50	f	wt	GBM	none	3.42 ± 0.06	-1.08 ± 0.29	1.6	-1.656 ± 0.014	2.31 ± 0.04	1.29	31.2 ± 1.1
11	M	69	р	wt	GBM	none	2.69 ± 0.07	-0.2 ± 0.3	1.53	-2.11 ± 0.04	1.69 ± 0.11	1.3	59. ± 7.
12	M	50	r	wt	GBM	none	1.29 ± 0.08	-0.3 ± 0.4	1.35	-2.78 ± 0.07	1.98 ± 0.18	1.16	$42. \pm 8.$
13	M	73	r	wt	A III	none	1.52 ± 0.05	0.84 ± 0.24	1.33	-2.8 ± 0.07	1.11 ± 0.19	1.33	$130. \pm 50.$
14	M	75	r	wt	GBM	none	1.43 ± 0.04	0.19 ± 0.19	1.41	-2.53 ± 0.04	2.11 ± 0.09	1.16	$37. \pm 3.$
15	M	66	r	wt	GBM	none	2.11 ± 0.04	0.84 ± 0.2	1.7	-2.103 ± 0.026	2.03 ± 0.07	1.22	40.4 ± 2.8
16	F	73	r	wt	GBM	none	2.57 ± 0.04	1.11 ± 0.2	1.48	-1.985 ± 0.017	1.98 ± 0.05	1.27	42.6 ± 1.9
17	F	58	f	mut	A III	none	3.24 ± 0.16	0.1 ± 0.7	1.77	-1.902 ± 0.028	1.66 ± 0.07	1.25	$60. \pm 5.$
18	F	31	р	mut	A III	none	2.76 ± 0.06	0.7 ± 0.28	1.6	-1.979 ± 0.019	1.73 ± 0.05	1.32	$56. \pm 3.$
19	M	43	р	mut	A III	none	1.83 ± 0.12	-0.9 ± 0.5	1.55	-2.47 ± 0.05	1.94 ± 0.15	1.23	44. ± 7.
20	F	33	p	mut	A III	none	1.56 ± 0.08	0.3 ± 0.4	1.63	-2.69 ± 0.04	1.44 ± 0.1	1.26	81. ± 11.
21	F	56	р	mut	ODG III	none	3.18 ± 0.1	-0.4 ± 0.4	1.71	-1.91 ± 0.03	1.78 ± 0.08	1.27	$53. \pm 5.$
22	M	34	p	mut	GBM	none	2.6 ± 0.07	0.2 ± 0.3	1.65	-2.109 ± 0.025	1.7 ± 0.07	1.18	$57. \pm 5.$
23	F	40	r	mut	A III	none	1.64 ± 0.04	1.05 ± 0.2	1.35	-2.69 ± 0.04	1.2 ± 0.11	1.28	$115. \pm 21.$
24	F	21	r	mut	A III	none	1.59 ± 0.09	0.7 ± 0.4	1.4	-2.72 ± 0.04	1.31 ± 0.1	1.15	$97. \pm 15.$
25	M	30	r	mut	A III	none	1.28 ± 0.07	1.1 ± 0.3	1.55	-2.96 ± 0.03	1.03 ± 0.09	1.23	$158. \pm 27.$
26	M	27	r	mut	A III	none	1.24 ± 0.11	-0.1 ± 0.5	1.46	-2.97 ± 0.05	1.54 ± 0.14	1.19	$70. \pm 13.$
27	M	59	r	mut	ODG III	none	1.63 ± 0.06	1.18 ± 0.3	1.62	-2.629 ± 0.025	1.29 ± 0.07	1.31	$101. \pm 11.$
28	M	22	r	mut	A II	none	1.77 ± 0.09	1.2 ± 0.4	1.61	-2.543 ± 0.028	1.33 ± 0.08	1.13	94. ± 11.
29	F	39	r	mut	ODG II	none	2.51 ± 0.1	2.6 ± 0.5	1.77	-2.168 ± 0.027	1.24 ± 0.07	1.34	109. ± 13.
30	M	40	r	mut	A III	none	1.85 ± 0.09	0.7 ± 0.4	1.46	-2.58 ± 0.03	1.27 ± 0.09	1.2	103. ± 14.
31	M	38	r	mut	A III	none	1.95 ± 0.1	-0.1 ± 0.4	1.36	-2.47 ± 0.05	1.63 ± 0.12	1.23	$63. \pm 9.$
32	F	28	r	mut	A III	none	2.61 ± 0.11	$3. \pm 0.5$	1.6	-2.128 ± 0.015	1.23 ± 0.04	1.2	$111. \pm 7.$
33	M	68	r	mut	GBM	OP/R/Ch	1.76 ± 0.14	1.2 ± 0.7	2.38	-2.41 ± 0.04	1.67 ± 0.11	1.21	$60. \pm 8.$

u(t) at t=0. u(t) reaches its maximum value $u_{max}=A/(e\cdot\kappa)$ for $t_{max}=TTP=\kappa^{-1/\beta}$. However, the model (3) is non-linear in its free parameters κ and β and therefore requires iterative algorithms for parameter fitting. A convergence of the iterative algorithms cannot be guaranteed and, since several iterations may be required, a long computation time in the case of voxel-wise curve fitting must be expected. A solution to the latter can be found due to the fact that the statistical distribution of the voxel values of PET images, which have been reconstructed using standard Maximum-Likelihood Expectation-Maximization (ML-EM), follows a log-normal distribution or gamma distribution instead of a normal distribution [22]-[25]. For low counts, and especially for timeframe durations lower than 1 minute, the gamma distribution is reported to better reproduce the image voxel value distribution [25]. All image frames included in the TAC analysis in this study are longer than 1 minute and show a high count rate, so that the log-normal distribution is assumed. Since the lognormal distribution is a heavy-tailed distribution [26], the requirement for least square regression, which assumes normally distributed error terms, is not fulfilled. However, the log-normal distribution can be transformed into a normal distribution by applying the natural logarithm to the random variable, in our case, the image voxel value [27]. The reader can readily check that (3) can be rewritten as

$$\ln(u(t)) = \ln(A) + \beta \cdot \ln(t) - \kappa \cdot t^{\beta} \tag{4}$$

by applying the logarithm to the equation. In the case that the free parameter β can be fixed to a value that universally holds for all uptake kinetics, (4) is linear in the remaining transformed fit parameters κ and $\ln(A)$, and is therefore accessible to noniterative linear regression methods without convergence problems. Furthermore, a fixed parameter β reduces the free fit parameters to two and lowers the parameter uncertainties. This allows the ¹⁸F-FET uptake behavior to be plotted in linearized graphs using t^{β} as abscissa and $\ln(u(t)) - \beta \cdot \ln(t)$ as ordinate. A preliminary evaluation revealed that the best choice of the free parameter β was close to 0.5 (average and standard deviation $\beta = 0.52 \pm 0.09$) for all cases and that, in the case of a model with three parameters (free β), the relative uncertainties are approximately one order of magnitude larger than for a model with two free parameters (β fixed). Owing to these findings and to the fact, that \sqrt{t} dependencies play a role in diffusion problems ([28], [29]), β was set to 0.5 for the remaining part of the present study and the time-to-peak value is given by $TTP_{Fit} = \kappa^{-2}$.

$$ln(u(t)) = ln(A) + 0.5 \cdot ln(t) - \kappa \cdot t^{0.5}$$
 (5)

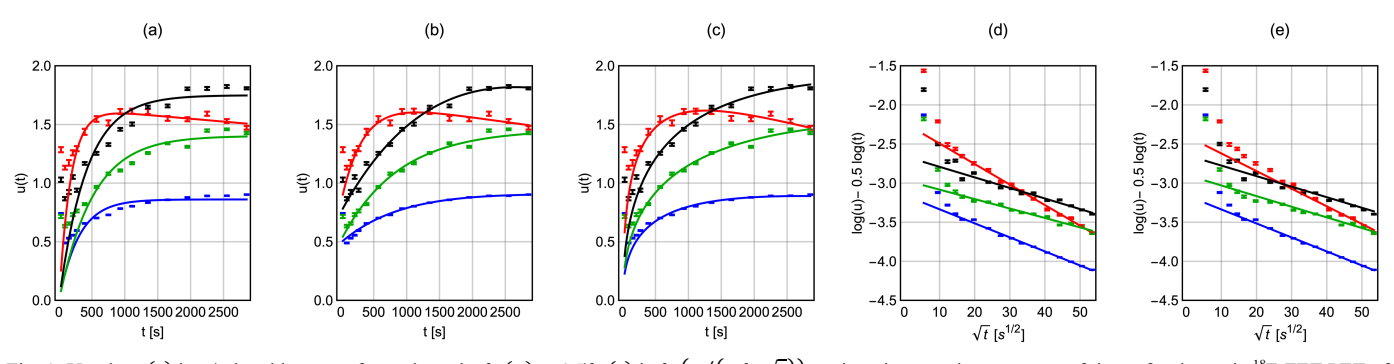


Fig. 1: Uptake u(t) in g/ml and log-transformed uptake ln(u) - 0.5ln(t) in $ln(g/(ml \cdot \sqrt{t}))$ against time t and square root of time t for dynamic ¹⁸F-FET PET of a patient with a recurrent, heterogeneous oligoastrocytoma of WHO grade II (test-case). The TACs were acquired in the 3T MR BrainPET insert. For this tumor, different ¹⁸F-FET uptake kinetic were observed in different tumor areas [15]. (a) Measured TACs and predictions obtained with the Bateman function (1) for 4 min < t < 50 min. (b) Measured TACs and predictions obtained with the double exponential model (2) for 4 min < t < 50 min. (c) Measured TACs and predictions obtained with the non-linear model (3) for β =0,5 for 4 min < t < 50 min. (d) Linearized TACs and fitted straight line for 4 min < t < 50 min. (e) Linearized TACs and fitted straight line for 20 min < t < 40 min. Blue: healthy control region, Green: TAC pattern "r", Black: TAC pattern "p", Red: TAC pattern "f".

As will be shown in section II, the models (3), (4), and (5) successfully reproduce all of the typically observed uptake kinetics for 18 F-FET. To allow comparison, the simple linear model [4], [13], [19] with slope m and y-axis intercept a was also used:

$$c(t) = m \cdot t + a \tag{6}$$

B. Data acquisition and PET image processing

¹⁸F-FET was produced with a specific radioactivity of > 200 GBq/µmol, a radiochemical yield of about 60-65%, and a radiochemical purity > 98% [30]. Approximately 237 \pm 28 MBq ¹⁸F-FET was administered as an isotonic neutral solution and all patients fasted for at least 4 h before the PET studies, in accordance with the German guidelines for brain-tumor imaging using radiolabeled amino acid analogs [31], [32]. Dynamic PET data from 0-50 min p.i. were acquired with a 3T MR-BrainPET hybrid system from Siemens Healthineers (axial FOV of the PET component, 19.2 cm). The Siemens 3T Magnetom Trio MR component of the MR-PET system was also used for providing MR derived, template-based attenuation correction maps for attenuation and scatter correction [33]. The PET data were stored as list-mode and were corrected for dead time, random coincidences, and radioactive decay. Iterative image reconstruction (vendor-provided OP-OSEM with two subsets and 32 iterations) was done for each of the 16 timeframes (5×1 min; 5×3 min; and 6×5 min). All emission images were scatter corrected (SSS) and motion-corrected with PMOD Technologies LLC software (rigid, square difference sums method), and a 2.5 mm, 3D-Gaussian filter was applied to the reconstructed images. Concentrations of ¹⁸F-FET in the tissue were converted to SUVs (g/ml) by dividing the radioactivity concentration (kBq/ml) in the tissue by the radioactivity injected per gram of body weight.

C. Patient population for verification

From April 2011 to April 2014, 33 adult patients (mean age, 50 ± 16 y, age range 21–75 y, 14 female patients), who were admitted for ¹⁸F-FET PET investigations due to a suspicion of

cerebral glioma or glioma recurrence following pretreatment were included in this study. Of the patients, 32 had primary tumors and one had a recurrent tumor. Histomolecular diagnosis according to the revised WHO classification of tumors of the central nervous system from 2016 [20] was available for all patients. In total, 16 newly diagnosed patients were diagnosed with IDH-wt gliomas (n=14 WHO grade IV glioblastoma; n=1 WHO grade III anaplastic astrocytoma; n=1 WHO grade II diffuse astrocytoma) and 17 patients with IDHmut gliomas (n=2 WHO grade IV glioblastoma; n=11 WHO grade III anaplastic astrocytoma; n=1 WHO grade II diffuse astrocytoma; n=2WHO grade Ш anaplastic grade oligodendroglioma; WHO II diffuse oligodendroglioma). Detailed patient characteristics summarized in Table I.

D. Evaluation of the linearized model (averaged TACs)

As a first step, the proposed model was tested for its ability to reproduce the different TAC patterns with sufficient agreement and the outcomes were compared to the two other non-linear models (1) and (2). This was achieved using an additional dynamic ¹⁸F-FET PET data set from a patient with a recurrent, oligoastrocytoma, not otherwise specified [15]. This patient was not included in the final analysis as the IDH status was not available. Throughout the remaining part of the paper, we will refer to this patient and the corresponding data set as test-case. For segmentation of the tumor volume, time-averaged PET images from 20-40 min p.i. were used. A 3D spherical background VOI with a constant size was positioned in the hemisphere contralateral to the lesion in healthy brain tissue (volume of background (BG) VOI: 14.1 ml; 7220 voxels; 30 mm diameter). The tumor volume was determined by a 3D auto-contouring process using a tumor-to-brain ratio of 1.6 or more in the averaged image [15]. VOIs with 15 mm diameter were manually placed in tumor areas of the test-case, which in a previous study showed different intratumoral tracer distributions between early (20-40 min p.i.) and late scans (70-90 min p.i.), e.g., hot spots in the early scan that disappeared in

the late scan and vice versa [15]. The tumor VOI and the spherical background VOI were stored and used to extract the corresponding image voxel values from all subjects and all time-frames. The natural logarithm of all voxel values in the tumor VOI and the healthy brain VOI was computed for all time-frames in order to transform the log-normally distributed PET image voxels into a normal distribution. Subsequently, the average of all voxel values within the same reconstruction timeframe and the same VOI, as well as the standard mean errors, were computed for original and logarithmized voxel values. The resulting TACs were linearized as described in section II-A and fitted using generalized linear regression to the model given in (5). The rather short bolus phase of FET cannot be adequately reproduced by a simple explicit model with only a few free parameters and, in addition, this time period is irrelevant for the aim of the presented study. Therefore, the PET images corresponding to the first four frames (0-240 seconds) of the dynamic acquisition, which are dominated by the bolus phase, were excluded from the regression.

For all cases, the best-fit parameters A and κ , their parameter uncertainties $\delta ln(A)$ and $\delta \kappa$, and χ^2/v for estimating the goodness of fit, were computed. In addition, the TTP_{Fit} value and uncertainty were computed for the best-fit parameters and by error progression, i.e. by using $\delta TTP_{Fit} = 2\kappa^{-3}\delta\kappa$ and $TTP_{Fit} = \kappa^{-2}$. The results were compared to the TAC patterns, to the fit results using the double exponential model (2), and to the late slope obtained from direct linear fits with model (6) of the TAC between 20 and 50 minutes p.i., as proposed in [4], [13], and [19]. In addition, the linearized model (5) and the linear model (6) were also evaluated for reduced data sets from 20-40 min p.i.. This short, total acquisition time is taken to represent datasets preferred in clinical settings.

E. Evaluation of the linearized model (voxel-wise)

For the evaluation of the voxel-wise uptake kinetics, the logarithms of all voxel values in the corresponding frames or VOIs were computed for all time-frames. Based on this, the TACs for all voxels were linearized as described in section II-D and fitted to the linearized model (4) using generalized linear regression. Again, the first four acquisition frames were excluded from the linear regression. ln(A), κ , $\delta ln(A)$, $\delta \kappa$, and χ^2/v were determined for all cases and all voxels. Averages of the obtained fit parameters were computed for the tumor and the BG VOI and were compared to the fit parameters obtained by fitting the average TAC. In addition, TACs for all image voxels of a single image slice for one representative IDH-mut and IDH-wt glioma were fitted, respectively. For comparison, the TAC intervals 20-50 min. p.i. for all voxels were fitted to the linear model (6) using linear regression.

F. Differentiation performance evaluation (average TAC)

Average TAC patterns of the tumor dynamics from 0 to 50 min p.i. were assigned by three independent clinical raters to one of the following curve patterns: constantly increasing ¹⁸F-FET uptake (rising, r), ¹⁸F-FET uptake peaking between 20 and 40 min followed by a plateau (plateau, p), and ¹⁸F-FET uptake peaking early (TTP < 20 min) followed by a constant descent (falling, f). The outcome of the Cohen's κ -test for measuring the degree of agreement among the raters was 0.46, which corresponds to good correlation. These pattern assignments were compared to classifications based on best-fit parameters obtained with averaged TACs and the models (6) and (5) for the acquisition intervals 4-50 min p.i. (linearized model), 20-50 min p.i. (linear model), and 20-40 min p.i. (both models). TTP_{Fit} values obtained via $TTP_{Fit} = \kappa^{-2}$ are listed together with the fit parameters for model (6), 20-50 min p.i. and model (4), 4-50 min p.i. in Table I. The diagnostic performance of m, a, A and κ for identification of IDH-wt gliomas was assessed by receiver-operating characteristics (ROC) analysis using the histomolecular confirmation as reference. Decision cutoff was considered optimal when the product of paired values for sensitivity and specificity reached its maximum. In addition, the area under the ROC curve (AUC), accuracy, and significance level were determined as a measure of diagnostic quality for both models (conventional linear TAC model and linearized TAC model) and for the different acquisition times. Leave-oneout cross-validation (LOOCV) was performed for validation of the prediction accuracy (cut-off value, sensitivity, specificity, accuracy, AUC, and χ^2/ν) and the false rate (FR) as a measure of predicted accuracy were computed. Differentiation between IDH-wt gliomas and IDH-mut gliomas was assessed with the ttest when the distribution of the parameters were normal and with the Mann-Whitney U-test otherwise. The correlation of voxel-wise best-fit parameters with the VOI based fit parameters and of best fit parameters for ln(A) and κ when comparing model (3) to model (4) were tested with the Pearson's correlation test (results given in supplementary tables and figures).

Table II: Best-Fit parameters, parameter uncertainties and χ^2/v for the four tacs in Fig. 1, and two acquisition intervals. In voi 1, a falling tac pattern was observed, in voi 2, a plateau tac pattern was observed and in voi 3, a rising tac pattern was observed.

Time interval	Region	ln(A)	κ [10-2/√s]	χ^2/ν
	Healthy ctrl.	-3.155 ± 0.016	1.8 ± 0.04	1.23
4 50 min n i	Tumor, VOI 1 (f)	-2.23 ± 0.023	2.63 ± 0.06	1.16
4-50 min p.i.	Tumor, VOI 2 (p)	-2.96 ± 0.03	1.21 ± 0.07	1.23
	Tumor, VOI 3 (r)	-2.66 ± 0.03	1.35 ± 0.08	1.23
	Healthy ctrl.	-3.157 ± 0.014	1.79 ± 0.03	2.32
20 40 min n i	Tumor, VOI 1 (f)	-2.4 ± 0.16	2.3 ± 0.4	2.35
20-40 min. p.i.	Tumor, VOI 2 (p)	-2.89 ± 0.21	1.4 ± 0.5	1.77
	Tumor, VOI 3 (r)	-2.64 ± 0.16	1.3 ± 0.4	1.66

III. RESULTS

A. Validation of the linearized model on the test-case

As a first validation, the TAC model was fitted to PET TACs from the *test-case* that presented regionally different tracer uptake kinetics (Fig. 1). In this single case, the fit was done for the time interval 4–50 min p.i.. The agreement observed

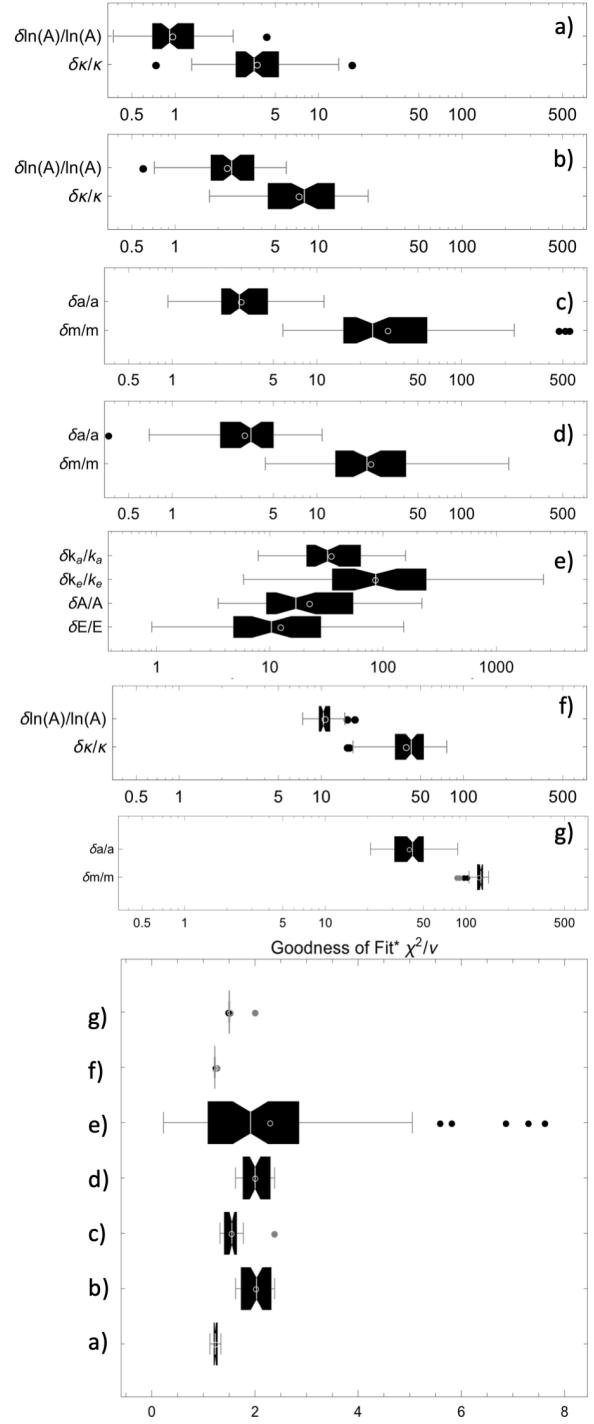


Fig. 2: Relative, estimated parameter uncertainties displayed by box-whisker charts for a) the proposed model (5), average TAC, and time interval 4–50 min p.i.; b) the proposed model (5), average TAC, and time interval 20–40 min p.i.; c) the linear model (6), average TAC, and time interval 20–50 min p.i.; d) the linear model (6), average TAC, and time interval 20–40 min p.i.; e) the double exponential model (2), average TAC, and time interval 4–50 min p.i.; f) the proposed model (5), voxel-wise TAC, and time interval 4–50 min p.i.; and g) the linear model (6), voxel-wise TAC, and time interval 20–50 min p.i.; The lower right plot shows the χ^2/v for all cases. All plots show min. and max. values (fences), inter quartile range (notched rectangle), median (notch), mean (circle), outlier (black dots), and far outlier (gray dots). *) For the Goodness of Fit plot, the χ^2/v values for the double exponential model were scaled down by 10 in order to allow visualization in the same plot.

between the adjusted model and the measured data was very good, with χ^2/ν values from 1.16 to 1.23 and relative, estimated parameter uncertainties smaller than 6% in all cases. For comparison, best fits obtained with the Bateman function and the double exponential model are also shown (Fig. 1). Although χ^2/ν values were between 1.32 and 1.4 for the Bateman function, systematic deviations from the measured TACs can clearly be observed in Fig. 1(a). Therefore, the Bateman function was excluded from further evaluations. Fits with the general double exponential model (2) achieved good visual agreement with the data and γ^2/ν values between 1.5 and 1.66. However, relative uncertainties of the estimated parameter are in the order of 100% for several parameters and cases. Fits with model (5) were repeated for the test case and reduced the acquisition time from 20-40 min p.i., resulting in slightly worse χ^2/ν values and relative uncertainties of the estimated parameter smaller or equal to 35%. However, when compared to best-fit parameters obtained with model (5) for intervals 20-40 min p.i. and 4-50 min p.i., the results were comparable within the corresponding fit-parameter uncertainty intervals. Fit results are given in Table II and supplementary Tables I-III. Average TACs of tumor VOIs and healthy control tissue VOI were also fitted with model (4) to evaluate the size of relative parameter uncertainties and correlation of ln(A), β , and κ for both models, which gave p < 0.001 and p = 0.005 respectively. All best-fit parameters for fits with model (4) are given in the supplementary Table IV.

B. Evaluation of the linearized model (averaged TACs)

When fitting the proposed linearized model (5) to the averaged TACs, best-fit parameters with small numerical parameter uncertainties (average 1% and 5% for both parameters, in all cases smaller than 20%) were obtained (see Table I and Fig. 2). The χ^2/ν values were between 1 and 1.5. When the simple linear model (6) was used together with the original TAC, numerical parameter uncertainties were, in all cases, larger by at least a factor of three. χ²/ν values were slightly larger (between 1.5 and 2.5). For the double exponential model (2), χ^2/ν values were significantly larger, reaching values close to 80. For this model, relative parameter uncertainties up to 1000% were unacceptably large. Thus, the double exponential model was excluded from further studies. When fitting the proposed linearized model (5) to the TACs in each individual voxel, best-fit parameter uncertainties were, on average, 10% for the amplitude parameter ln(A) and 40% for κ , respectively. χ^2/ν values were comparable to the case where the average TACs were fitted. Best-fit parameters, uncertainties, and χ^2/ν for the proposed linearized model (5) for its maximal possible time interval 4-50 min p.i. are given in Table I along with the results obtained with the linear model (6) for its maximal possible time interval 20-50 min p.i.. The histological grading and the TTP values obtained from $TTP_{Fit} = \kappa^{-2}$ are also shown in Table I. Using the computation from κ allows a

valid TTP value to be also obtained for TAC patterns r and p. In addition, best-fit parameters obtained from the linearized model for 4-50 min p.i. and from the linear model for 20-50 min p.i. were compared to the observed TAC patterns (see Fig. 4). The significances of the separation between the three groups (pattern r vs. pattern p; pattern p vs. pattern f; and pattern r vs. pattern f) were: 0.1, < 0.001, and < 0.001 for κ ; 0.04, 0.002, and < 0.001 for $\ln(A)$; 0.009, 0.001, and < 0.001 for m; and 0.01, 0.09, and < 0.001 for a, respectively. As expected, no differentiation was possible for the best-fit parameters obtained from the fitted averaged TACs of the healthy background VOI.

Results for the ROC analysis of parameter κ (obtained from average TACs) with LOOCV are given in Table III. The best differentiation between IDH-wt and IDH-mut gliomas was achieved with the linearized model fitted to the averaged TAC values from 4-50 min p.i. Accuracy, sensitivity, AUC, and FR were considerably worse for the standard linear model fit to the TAC values from 20-50 min p.i.. When the acquisition time was limited to 20-40 min p.i. to test the potential application of the method in common clinical settings, classification accuracy and specificity was slightly lower for both models, while the sensitivity and AUC were slightly better in case of the linear model. A comparison of the different acquisition intervals showed that the cut-off values for the proposed linearized model do not vary within the estimated uncertainty interval. An ROC analysis for a combination of both best-fit parameter values (κ with A and m with a, respectively) through logistic regression or by building a ratio (motivated by the fact that the value $u_{max} = A/(e \cdot \kappa)$ is reached at $t = TTP_{Fit}$) did not further improve the classification accuracy.

C. Evaluation for voxel-wise TACs (cross validation)

When fitting the linearized model to the individual TAC of each PET image voxel, the best-fit parameter uncertainties were, as expected, larger than in the averaged TAC case but still within an acceptable range. In the case of ln(A), the uncertainties were, on average, 10% for ln(A) and 40% for κ . The averaged values of ln(A) and κ obtained from the fits per Table III: Cut-off values, accuracy, sensitivity, specificity, false rate, auc, and significance for the differentiation between IDH-wt and IDH-mut gliomas obtained from roc analysis with the 33 patients for linearized, linear model, and different acquisition intervals.

	Linearized	Standard linear	Linearized	Standard linear
Measure	model, 4-50	model, 20-50	model, 20-40	model, 20-40
	min p.i.	min p.i.	min p.i.	min p.i.
Cut-off [10-3]	18.33 ± 0.23	-0.0164 ± 0.001	18.2 ± 1.2	-0.0879 ± 0.0013
Acc. [%]	91 ± 1	85 ± 1	79 ± 2	82 ± 1
Sens. [%]	88 ± 2	75 ± 2	94 ± 10	81 ± 2
Spec. [%]	94 ± 1	94 ± 1	65 ± 11	82 ± 2
FR [%]	12	15	39	24
AUC [%]	92 ± 1	84 ± 1	88 ± 1	87 ± 1
p-value	< 0.001	< 0.001	< 0.001	< 0.001
χ^2/ν	1.239 ± 0.009	1.556 ± 0.035	2.01 ± 0.05	2.01 ± 0.05

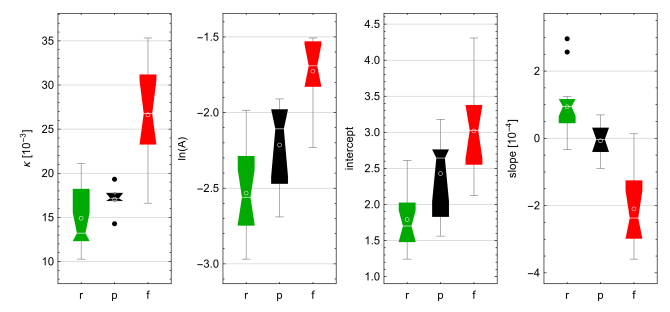


Fig. 3: κ , ln(A), m, and a values depending on the TAC pattern in tumor tissue. Plots show min. and max. values (fences), inter quartile range (notched rectangle), median (notch), mean (circle), and outlier (dot). No significant differentiation was observed for the healthy tissue. Colors as in Fig. 1.

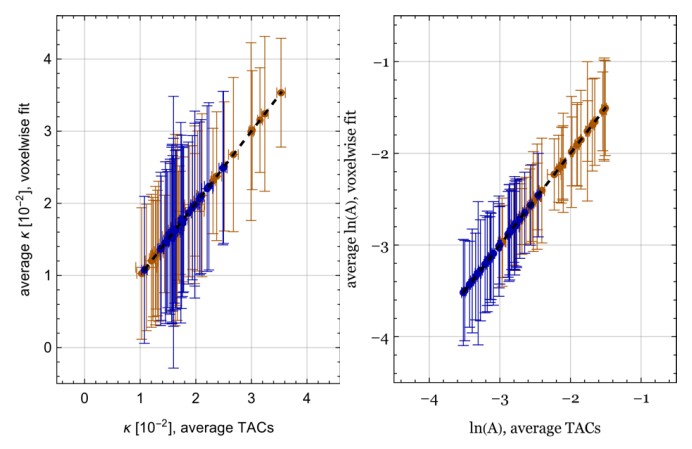


Fig. 4: Best-fit parameters obtained from fitting averaged TACs (abscissa) vs. average of best-fit parameters obtained from voxel-wise fits (ordinate) for κ (left) and ln(A) (right). All 3 patterns are shown together. Orange dots: tumor tissue. Blue dots: healthy control tissue. Error bars represent parameter uncertainties (ordinate) and standard deviations (abscissa).

of ln(A) and κ obtained from fitting the averaged TACs of the 33 data sets (see Fig. 3). Dependency tests (Pearson correlation) gave values significantly smaller than 0.001 for ln(A) and κ . The average required time per fit was approx. 2 ms on an Intel Core i7-4980HQ processor at 2.8 GHz (using high-level languages without parallelization and without optimizing code for speed). Fitting all image voxels in one PET image slice with 256×256 voxels required approx. 1 min (image voxels corresponding to the air surrounding the subject were excluded). In Fig. 5, best-fit parameters, relative parameter uncertainties and χ^2/ν are shown as parametric images. The corresponding histograms for one image slice from one patient with IDH-wt GBM and one patient with IDH-mut diffuse astrocytoma are also shown. In addition, the averaged SUV values corresponding to the data acquisition from 20-40 min p.i. are given for comparison. While the IDH-wt GBM can be recognized easily on the image with the averaged SUV values and both parametric images (ln(A) and κ), the IDH-mut diffuse astrocytoma is only visible on the image with the averaged SUV values. The histograms for ln(A) and κ show a clear shift towards larger values in the case of the IDH-wt GBM compared to the values of the healthy control tissue. In the case of the IDH-mut diffuse astrocytoma, ln(A) values are only slightly

shifted towards higher values and the κ values are shifted towards smaller values. Relative parameter uncertainties are also shown in Fig. 5 (3rd and 4th row). It can be seen that the relative parameter uncertainties tend to be smaller for TACs in regions with higher uptake. The χ^2/ν values are homogeneously distributed, thus showing that the proposed model describes the measured data well for all tissue types. Corresponding parametric images were produced with the linear model (6) for the acquisition interval 20-50 min p.i. and are shown in supplementary Fig. 1. While a differentiation between the IDH-wt GBM case and the IDH-mut diffuse astrocytoma case is still possible with the parametric images for *a* and *m*, the noise level of the images and the parameter uncertainties are higher compared to the ones obtained with the linearized model (5).

IV. DISCUSSION

One aim of this study was to evaluate the numerical robustness of a rather simple linearized fit model for TACs obtained from dynamic ¹⁸F-FET PET studies. In addition, we evaluated the precision of the differentiation between IDH-wt and IDH-mut gliomas using the best-fit parameter κ , which describes the TAC shapes. We compared the results to already existing methods such as fitting the late slope using a linear model and visual inspection by experienced physicians. The highest diagnostic accuracy (91%) for the identification of IDH-wt gliomas was achieved using the linearized model (5) over the acquisition interval 4-50 min p.i. together with averaged TACs, since, in this case, the number of TAC data points used for the fit was maximal. This accuracy is comparable to values previously achieved with the aforementioned alternative methods for averaged TAC shape discrimination [6], [8], [14], [34]. Interestingly, the classification accuracy obtained with the linear model on data acquired from 20-40 min p.i. and averaged TACs is comparable to the accuracy obtained with the linearized model for the same time interval. This can be explained by the near-linear behavior of the TACs within this shorter time interval and the small number of data points, i.e. only four values. A reduction of the time-frame length to 1 min or 2 min did not result in an improvement for either of the models; however, we attribute this to the fact that the frames were too short for reliable motion correction. A follow-up study is planned, where the impact of frame lengths with durations between 2 and 5 min will be further investigated. Relative fit parameter uncertainties for fitting the averaged TACs with the linearized model were smaller than 20% in all cases and are therefore acceptable. In corresponding cases with the linear model, the relative fit parameter uncertainties were larger by at least a factor of three. When the linearized model was fitted to the TAC of the individual voxels, the parameter uncertainties considerably larger. This was as expected. However, in 75% of the cases, they were smaller than $\approx 50\%$ and $\approx 13\%$ for $\delta\kappa/\kappa$ and $\delta ln(A)/ln(A)$, respectively. Average fit parameters obtained from voxel-wise fits correlate strongly with the fit parameters obtained from fitting the averaged TACs for corresponding cases. Owing to the transformation of the model into a linearized model, the processing speed is high, convergence issues need not be considered, and parametric images for κ and ln(A) could be computed without supervision in approx. 60 seconds per image slice (256×256 voxels). To the best of our knowledge, only a small number of alternative voxel-based tumor grade classification approaches have been reported to date [13], [14], and [19]. Blanc-Durand et al. [14] developed an automatic method to cluster the TAC from ¹⁸F-FET PET acquisitions into three characteristic curve shapes. However, in the presented approach κ represents a continuous parameter, that is not limited a priori to a fixed number of reference curves. Vomacka et al. [13] determined the TTP by selecting the maximum TAC value after 2.7 min. p.i and performed voxelwise fits with model (6) for the acquisition interval from 15-40 min p.i.. Göttler et al. [19] performed voxel-wise fits with model (6) for the acquisition interval from 10-30 min p.i. All three groups focused on how to use the voxel-wise classification of TTP, slope, and curve shape for the classification of tumor malignancy. In contrast, the focus of our study was to provide a general, robust model with low parameter uncertainties to enable automatic, un-supervised and objective parametrization of ¹⁸F-FET PET TAC curve patterns. In particular, the use of model (5) leads to a parametrization that allows a direct comparison when using different acquisition intervals. This is not possible when using the linear model (6). Also, when differentiating between WHO grades II and III and WHO grade IV, as done in Vomacka et al. [13] and Lohmann et al. [15], very similar differentiation accuracy is achieved when using parameter κ of model (5).

A further important finding from the study is that the continuous parameter κ of model (5) also allows TTP values to be accessed when the peak of the TAC is reached after the PET acquisition has been stopped. This is achieved by using the relationship $TTP_{Fit} = \kappa^{-2}$. The differences in TPP values for the IDH-mut glioma group (average: 84 min, std. dev: 30 min., min: 44 min, max: 158 min.) and the IDH-wt glioma group (average: 37 min, std. dev: 38 min., min: 13.4 min, max: TTP0 min.) were significant (p < 0.001). Average TPP values for comparable groups reported by Vomacka *et al.* [13] and Röhrich *et al.* [35] were considerably lower than in the presented case. We attribute this to a bias towards smaller values for TTP, which is introduced when determining the TPP value as the maximum of the measured TAC.

Although the linearized model was based on very general observations, an interpretation of both fit parameters is of great interest. An important observation is that the case $\kappa=0$ exists and yields in this limit a simple square root kinetics $\mathbf{u}(t)=A\sqrt{t}$. Although the \sqrt{t} dependency plays a role in diffusion problems [28], [29], we do not understand this similarity at present. At the same time, $e^{-\kappa\sqrt{t}} \leq 1 \forall t \geq 0$ and therefore switching κ on $(\kappa>0)$ always yields a lower uptake than in the case $\kappa=0$ and the same A parameter. Thus, in our model, $\kappa>0$ represents a reduced uptake or, alternatively, an extraction of the tracer or its radioactive metabolites from the tumor volume. In an alternative, but equivalent formulation of model (5), the argument of the exponential function could be rewritten as $e^{-\sqrt{\kappa \cdot t}}$. In this case, the shape parameter κ has the dimension

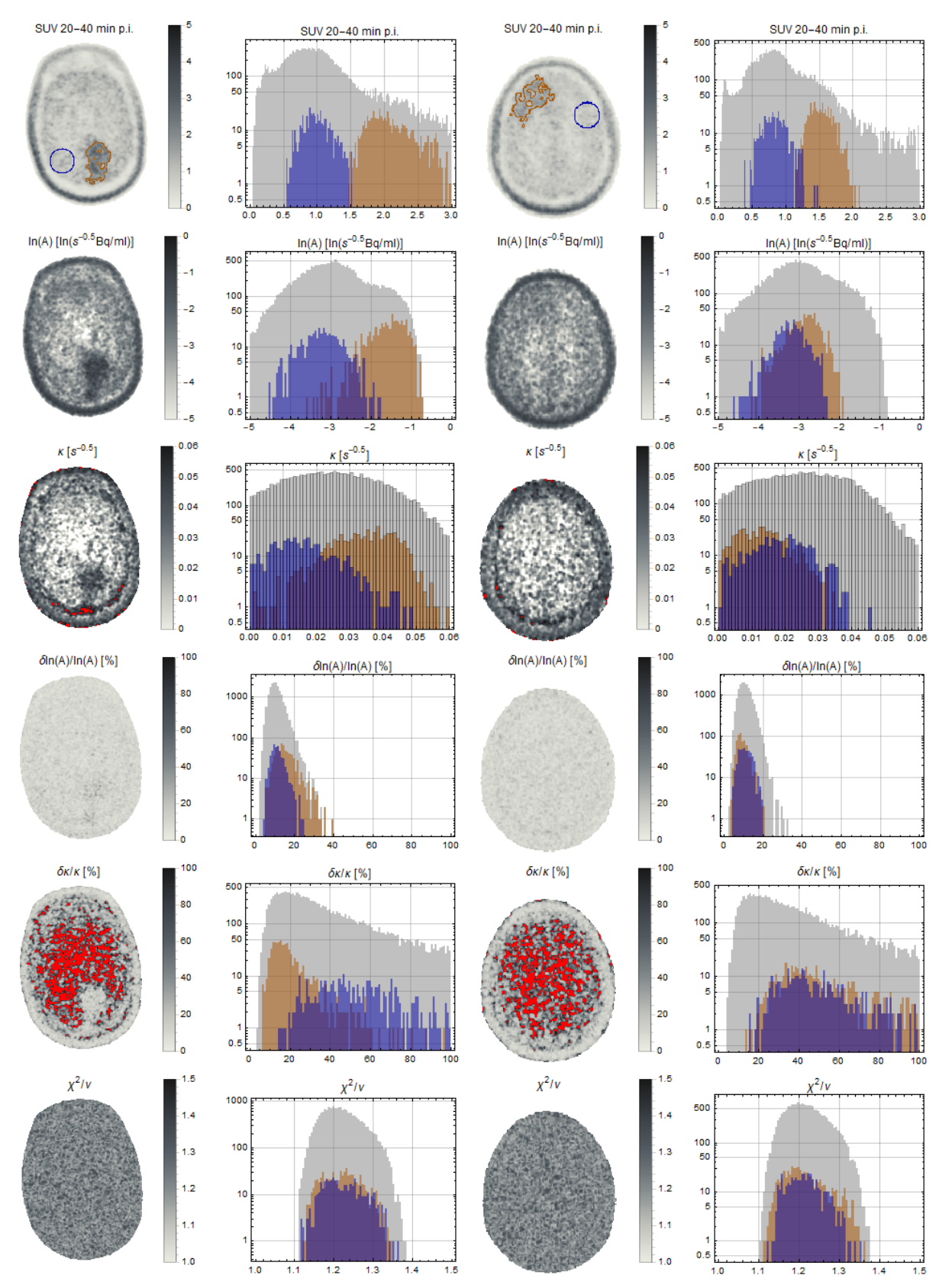


Fig. 5: Parametric images for one patient with an IDH-wt glioblastoma (subject 1, left column) and one patient with an IDH-mut diffuse astrocytoma (subject 25, right column). First row shows average SUV image from 20-40 min p.i. (in the SUV images, the healthy control region is marked as blue contour and the tumor region is marked as orange contour). Second and third rows show parametric image for $\ln(A)$, parametric image for κ and corresponding voxel value histograms. Gray shaded bins represent all image voxels (except voxels outside the object), blue bins represent voxels in the healthy control region and orange bins represent voxels in the tumor regions. In the fourth, fifth, and sixth row, corresponding relative parameter uncertainties and χ^2/ν are shown. Voxel values exceeding the plot range are highlighted with red color.

 s^{-1} and could be compared to the elimination rates k_2 for the 1-tissue compartment model and the k_2 and k_4 values for the 2-tissue compartment model. This is in agreement with the observation that 18 F-FET is not significantly incorporated into any metabolic pathway and the uptake appears to be governed by transport [36]. However, the mechanism that leads to different 18 F-FET TAC shapes is not yet fully understood and may reflect many aspects of brain tumors. For example, Habermeier et al. state, that 18F-FET is trapped inside LAT1-expressing cells due to very poor efflux [37], which would not be compatible with the falling pattern and κ values significantly larger than 0. Liesche *et al.* found a significant correlation between the amount of neovascularization and the 18 F-FET TAC slopes [38].

Unfortunately, the number of studies applying pharmacokinetic analysis based on compartment models in brain tumors is low [7], [11], [12], [35], and [39]. Numerical values for the parameters are in the same order of magnitude, e.g., rate constants reported in [39] are between 2×10⁻²/min and 100×10^{-2} /min, which approximately correspond to $0.018/\sqrt{sec}$ and $0.13/\sqrt{sec}$. A more detailed comparison is not possible, since Debus et al. limit their study [39] to HGG, Koopman et al. do not report values for all rate constants [11], [12], Thiele et al. do not compare rate constants for different tumor grades. and Röhrich et al. [35] only report relative k₁, k₂ and k₃ values. Kratochwil et al. do report all rate constants, and report, consistent with our findings, higher elimination rates (k₂ and k₄) for GBM [7]. However, they did not find significant tumor grade dependent differences for the elimination rate constants. We are currently studying the relationship between κ and the k_2 and k₄ values for the 2-tissue compartment model in detail. These results and additional applications for the parametric images obtained with the model will be presented in subsequent publications.

A final remark should be made on taking the logarithm of the image voxel values to transform their log-normal distribution into a normal distribution. In general, a Gaussian filter is applied to PET images reconstructed with the ML-EM algorithm to reduce the image noise. This was verified by analyzing reconstructed and smoothed PET images from a homogeneous phantom, and it was found that the resulting voxel value distribution is still log-normal and therefore the logarithm can be applied to the voxel values. However, extracted fit parameter values and errors, χ^2/v , and classification results could still be used dependent on the width of the Gauss filter. Finally, log-normal distributions were also observed in the cellular uptake of radioactivity, as quantified by autoradiography without ML-EM image reconstruction [40].

V. CONCLUSIONS

We present a linearized fit model for dynamic ¹⁸F-FET PET studies which enables fast, automatic, and numerically robust voxel-wise characterization of TAC shapes. The method provides a continuous and objective scalar parameter that describes the TAC shape and was successfully validated in a clinical dataset in patients with IDH-wt and IDH-mut gliomas. When compared to alternative fit-models, the best classification of gliomas into IDH-wt and IDH-mut was achieved with the

linearized model fitted to the averaged TAC values from dynamic FET PET data in the time interval 4-50 min p.i. Compared to other possible models, the proposed linearized model achieves good agreement with measured TACs, has only two free parameters, and can be linearized, thus providing increased numerical stability and lower parameter uncertainties, especially in the case of voxel-wise analysis. We also showed that the classification performance of the linearized fit model and the standard linear fit model were only slightly lower for the reduced acquisition interval 20–40 min p.i. The method can, therefore, also be used in clinical settings.

ACKNOWLEDGMENT

The authors thank Silke Frensch, Suzanne Schaden, Inês Monteiro Costa, and Sujeethadevi Purushothaman-Lalitha for their help with image processing. Claire Rick is thanked for her editorial input and proofreading of the manuscript.

REFERENCES

- K. J. Langen, N. Galldiks, E. Hattingen, and N. J. Shah, "Advances in neuro-oncology imaging", Nat. Rev. Neurol, vol. 13, no. 5, pp. 279-289, 2017.
- [2] D. N. Louis et al., "The 2007 WHO classification of tumours of the central nervous system," Acta Neuropathologica, vol. 114, no. 2. Springer, pp. 97-109, Aug. 06, 2016.
- [3] F. Vettermann et al., "Non-invasive prediction of IDH-wildtype genotype in gliomas using dynamic 18F-FET PET," Eur. J. Nucl. Med. Mol. Imaging, vol. 46, no. 12, pp. 2581–2589, Nov. 2019.
- [4] A. Verger et al., "Static and dynamic 18F-FET PET for the characterization of gliomas defined by IDH and 1p/19q status," Eur. J. Nucl. Med. Mol. Imaging, vol. 45, no. 3, pp. 443–451, Mar. 2018.
- [5] G. Pöpperl et al., "Analysis of 18F-FET PET for grading of recurrent gliomas: Is evaluation of uptake kinetics superior to standard methods?," J. Nucl. Med., vol. 47, no. 3, pp. 393–403, Mar. 2006.
- [6] G. Pöpperl et al., "FET PET for the evaluation of untreated gliomas: Correlation of FET uptake and uptake kinetics with tumour grading," Eur. J. Nucl. Med. Mol. Imaging, vol. 34, no. 12, pp. 1933–1942, Dec. 2007
- [7] C. Kratochwil et al., "Intra-individual comparison of 18F-FET and 18F-DOPA in PET imaging of recurrent brain tumors," Neuro. Oncol., vol. 16, no. 3, pp. 434–440, 2014.
- [8] G. Moulin-Romsée et al., "Non-invasive grading of brain tumours using dynamic amino acid PET imaging: Does it work for 11C-Methionine?," Eur. J. Nucl. Med. Mol. Imaging, vol. 34, no. 12, pp. 2082–2087, Dec. 2007.
- [9] Y. Nomura et al., "Characteristics of time-activity curves obtained from dynamic 11 C-methionine PET in common primary brain tumors," J. Neurooncol., vol. 138, no. 3, pp. 649–658, Jul. 2018.
- [10] M. Ginet et al., "Integration of dynamic parameters in the analysis of 18F-FDopa PET imaging improves the prediction of molecular features of gliomas," Eur. J. Nucl. Med. Mol. Imaging, vol. 47, no. 6, pp. 1381– 1390, Jun. 2020.
- [11] F. Thiele, et al. "The quantification of dynamic FET PET imaging and correlation with the clinical outcome in patients with glioblastoma". Phys. Med. Biol., vol. 54, no. 18, p. 5525, 2009.
- [12] T. Koopman et al., "Quantification of O-(2-[18F]fluoroethyl)-L-tyrosine kinetics in glioma," EJNMMI Res., vol. 8, no. 1, p. 72, Dec. 2018.
- [13] L. Vomacka et al., "Voxel-wise analysis of dynamic 18F-FET PET: a novel approach for non-invasive glioma characterisation," EJNMMI Res., vol. 8, no. 1, pp. 1–13, Sep. 2018.
- [14] P. Blanc-Durand et al., "Voxel-based 18 F-FET PET segmentation and automatic clustering of tumor voxels: A significant association with IDH1 mutation status and survival in patients with gliomas," PLoS One, vol. 13, no. 6, Jun. 2018.
- [15] P. Lohmann et al., "Dual-time-point O-(2-[18F]fluoroethyl)-L-tyrosine PET for grading of cerebral gliomas," Eur. Radiol., vol. 25, no. 10, pp. 3017–3024, Oct. 2015.

- [16] W. Paulus and J. Peiffer, "Intratumoral histologic heterogeneity of gliomas. A quantitative study," Cancer, vol. 64, no. 2, pp. 442–447, Jul. 1989
- [17] J. C. L. Alfonso et al., "The biology and mathematical modelling of glioma invasion: A review," Journal of the Royal Society Interface, vol. 14, no. 136. Royal Society Publishing, Nov. 01, 2017.
- [18] M. Kunz et al., "Hot spots in dynamic18FET-PET delineate malignant tumor parts within suspected WHO grade II gliomas," Neuro. Oncol., vol. 13, no. 3, pp. 307–316, 2011.
- [19] J. Göttler et al., "Intra-lesional spatial correlation of static and dynamic FET-PET parameters with MRI-based cerebral blood volume in patients with untreated glioma," Eur. J. Nucl. Med. Mol. Imaging, vol. 44, no. 3, pp. 392–397, Mar. 2017.
- [20] D. N. Louis et al., "The 2016 World Health Organization Classification of Tumors of the Central Nervous System: a summary," Acta Neuropathologica, vol. 131, no. 6. Springer Verlag, pp. 803–820, Jun. 01, 2016.
- [21] S. C. Khojasteh, H. Wong, and C. E. C. A. Hop, Drug Metabolism and Pharmacokinetics Quick Guide. Springer New York, 2011.
- [22] H. H. Barrett, D. W. Wilson, and B. M. W. Tsui, "Noise properties of the EM algorithm. I. Theory - IOPscience," Phys. Med. Biol., vol. 39, no. 5, p. 833, 1994.
- [23] D. W. Wilson, B. M. W. Tsui, and H. H. Barrett, "Noise properties of the EM algorithm. II. Monte Carlo simulations - IOPscience," Phys. Med. Biol., vol. 39, no. 5, p. 847, 1994.
- [24] J. A. Thie, K. F. Hubner, and G. T. Smith, "The diagnostic utility of the lognormal behavior of PET standardized uptake values in tumors," J. Nucl. Med., vol. 41, no. 10, pp. 1664–1672, Oct. 2000.
- [25] T. Mou, J. Huang, and F. O'Sullivan, "The gamma characteristic of reconstructed pet images: Implications for ROI analysis," IEEE Trans. Med. Imaging, vol. 37, no. 5, pp. 1092–1102, May 2018.
- [26] K. Sigman, "A primer on heavy-tailed distributions," Queueing Syst., vol. 33, no. 1–3, pp. 261–275, 1999.
- [27] E. Limpert, W. A. Stahel, and M. Abbt, "Log-normal Distributions across the Sciences: Keys and Clues On the charms of statistics, and how mechanical models resembling gambling machines offer a link to a handy way to characterize log-normal distributions, which can provide deeper insight into variability and probability—normal or log-normal: That is the question," Bioscience, vol. 51, no. 5, pp. 341–352, May 2001.
- [28] J. Crank, "The mathematics of diffusion. 2nd Edn.," pp. 1-421, 1979.

- [29] J. Siepmann and N. A. Peppas, "Higuchi equation: Derivation, applications, use and misuse," International Journal of Pharmaceutics, vol. 418, no. 1. Elsevier, pp. 6–12, Oct. 10, 2011.
- [30] K. Hamacher and H. H. Coenen, "Efficient routine production of the 18F-labelled amino acid O-(2-[18F]fluoroethyl)-L-tyrosine," Appl. Radiat. Isot., vol. 57, no. 6, pp. 853–856, Dec. 2002.
- [31] K. Langen et al., "German guidelines for brain tumour imaging by PET and SPECT using labelled amino acid," Nuklearmedizin, vol. 50, no. 4, pp. 167–173, 2011.
- [32] I. Law et al., "Joint EANM/EANO/RANO practice guidelines/SNMMI procedure standards for imaging of gliomas using PET with radiolabelled amino acids and [18 F]FDG: version 1.0," Eur. J. Nucl. Med. Mol. Imaging, vol. 46, no. 3, pp. 540–557, Mar. 2019.
- [33] H. Herzog et al., "High resolution BrainPET combined with simultaneous MRI," Nuklearmedizin, 2011.
- [34] N. L. Jansen et al., "MRI-suspected low-grade glioma: Is there a need to perform dynamic FET PET?," Eur. J. Nucl. Med. Mol. Imaging, vol. 39, no. 6, pp. 1021–1029, Jun. 2012.
- [35] M. Röhrich et al., "Integrated analysis of dynamic FET PET/CT parameters, histology, and methylation profiling of 44 gliomas," Eur. J. Nucl. Med. Mol. Imaging, vol. 45, no. 9, pp. 1573–1584, Jul. 2018.
- [36] K. J. Langen et al., "O-(2-[18F]fluoroethyl)-l-tyrosine: uptake mechanisms and clinical applications," Nuclear Medicine and Biology, vol. 33, no. 3. Elsevier, pp. 287–294, Apr. 01, 2006.
- [37] A. Habermeier, J. Graf, B. F. Sandhöfer, J. P. Boissel, F. Roesch, and E. I. Closs, "System I amino acid transporter LAT1 accumulates O-(2fluoroethyl)-I-tyrosine (FET)," Amino Acids, vol. 47, no. 2, pp. 335–344, Nov. 2015.
- [38] F. Liesche et al., "18F-Fluoroethyl-tyrosine uptake is correlated with amino acid transport and neovascularization in treatment-naive glioblastomas," Eur. J. Nucl. Med. Mol. Imaging, vol. 46, no. 10, pp. 2163–2168, Sep. 2019.
- [39] C. Debus et al., "Feasibility and robustness of dynamic 18F-FET PET based tracer kinetic models applied to patients with recurrent high-grade glioma prior to carbon ion irradiation," Sci. Rep., vol. 8, no. 1, pp. 1–17, Dec. 2018.
- [40] P. V. S. V. Neti and R. W. Howell, "Log normal distribution of cellular uptake of radioactivity: Implications for biologic responses to radiopharmaceuticals," J. Nucl. Med., vol. 47, no. 6, pp. 1049–1058, 2006.